

---

# Simulation of Submicrometer Metal–Semiconductor–Metal Ultraviolet Photodiodes on Gallium Nitride

## Introduction

Due to the high steady-state peak electron velocity<sup>1–4</sup> in gallium nitride (GaN) and the simplicity of fabrication, metal–semiconductor–metal photodiodes (MSM-PD's) fabricated on GaN have attracted intensive research effort. High-bandwidth, monolithic MSM devices have already been demonstrated.<sup>5–8</sup> Both Monte Carlo simulations<sup>9</sup> and experimental measurements<sup>10</sup> have shown that the intrinsic response time of the GaN MSM-PD's could be as fast as a few picoseconds. For practical applications, however, it is necessary to integrate the device into a fast package so that the photogenerated signal can be coupled out to standard timing instruments, such as a fast oscilloscope or a readout circuit. The packaging process will inevitably introduce a parasitic effect that limits the high-frequency performance of the devices. Our previous experimental results<sup>5</sup> showed the dominant role of the packaging fixture. To identify the performance-limiting factors and to design MSM-PD's with a required bandwidth and responsivity, it is essential to examine the dynamic behavior of the integrated unit including the photodiode and the packaging circuit.

In MSM-PD's, there are several design considerations in trying to improve their speed of response. Decreasing the inter-electrode spacing has the beneficial effect of decreasing carrier-transit time (which decreases the response time), at the cost of an increase in the device capacitance (which increases the response time). To reduce the device capacitance, one can reduce the area of the interdigitated fingers. This requires a tighter focusing of the incident beam. Shrinking the total detector area would also increase the current density; thus the maximum total charge that can be delivered to the processing electronics must decrease. As a result, it is necessary to understand the behavior of UV MSM-PD's under a wide range of illumination levels. The transient behavior of infrared MSM-PD's subjected to optical pulse energies ranging from 0.01 to 316 pJ was reported recently.<sup>11</sup> The pulse broadening under high optical energy was attributed to the space-charge screening effect, which was studied in Refs. 12 and 13 for GaAs. However, theoretical simulations and experimental studies of the screening effect in GaN MSM-PD's under high illumina-

tion conditions have not appeared in the literature. This effect is part of our study and will be discussed in detail below.

## Simulation

The MSM device with 0.3- $\mu\text{m}$  feature size and the broad-band circuit to be simulated are the same as reported previously<sup>5</sup> (see Fig. 99.80). The circuit has a strip-line structure with the switch attached on a G-10 board. At first, we tried to model the entire assembly by an equivalent circuit with the lumped electric elements and then solve the circuit by using *SPICE*. This approach is simple and straightforward. The photocurrent, however, must be input as a parameter rather than calculated directly. Therefore the model cannot explore the opto-electronic process that occurs under optical illumination. Furthermore, this method cannot monitor the circuit effect and space-charge screening effect as discussed below.

To better understand the transient behavior of the device, we developed a more-complicated numerical simulation using a distributed-circuit approach.<sup>14–16</sup> Similar simulations have been used to describe the electric field in high-voltage photoconductive switches, although this is the first time they have been applied to an MSM photodiode. Instead of tracking the detailed carrier dynamics,<sup>12,13</sup> we assume that the optically generated electron-hole pairs are swept out (with negligible recombination) at rates determined by the field-dependence velocities.<sup>1</sup> The transient current and voltages are computed simultaneously and dynamically to produce the device temporal response. A major advantage of this approach is that it allows us to conveniently include the effect of the packaging circuit.

The simulation assumes a transverse electromagnetic wave propagation. This is an approximation that ignores modal dispersion and the discontinuity in the dielectric constant between the strip line and the air. The entire circuit, including the charge source, the transmission line, the semiconductor, and the load, was sliced into 1024 small cells along the equipotential lines. Each cell is modeled by discrete elements: resistors, capacitors, and inductors (see Fig. 99.80;  $k$  is an even number) whose values are computed from the cell geometry.<sup>17</sup>

All of the cells have identical configurations and are linearly coupled to the two adjacent neighbors; therefore, we need to focus on solving only one such cell, and then the equations for the entire circuit can be mapped out. In each cell, only two unique nodes are considered: an “even” node and an “odd” node, as shown in Fig. 99.81, where  $R_t$  is the resistance of the small cell, the value of which depends on the material properties of the location and is photosensitive in the active area of the device;  $C_s$  is the capacitance across the resistance;  $C_g$  is the capacitance between the cell and the ground;  $L_s$  is the inductance of the cell; and  $V_k$  is the potential at each node. When the Kirchhoff’s law of current continuity is applied to these nodes, the equations of voltage and current can be obtained.

Several assumptions were made in deriving the circuit equations: (1) The Schottky contact in MSM-PD’s is non-injecting; that is, no electron can flow from metal cell to semiconductor cell on the boundary between materials. (2) The gap between fingers is fully depleted, resulting in high resistivity; this is justified by noting that the flatband<sup>18</sup> voltage across the gap is calculated to be 0.25 V, much lower than the applied bias voltage of 5 V. (3) The optical illumination is spatially uniform across the finger spacing since the size of the spacing ( $0.3 \mu\text{m}$ ) is much smaller than that of the active area ( $50 \mu\text{m}$ ) and the focal spot ( $\sim 10 \mu\text{m}$ ). (4) The 2-D dependence of the electric

field is neglected, and the electric field is uniform across the finger gap of the devices. This 1-D simulation appears to be a good approximation in estimating the device response time.

It is worthwhile to note that a more fundamental approach detailing the carrier dynamics has been done previously<sup>12,13</sup> using a numerical Poisson solver. In the simplified, distributed-circuit approach presented here, the entire package was modeled by discrete circuits. While it is straightforward to describe the rest of the circuit, it took some effort to build the accurate model for the interdigitated MSM photodiode so that

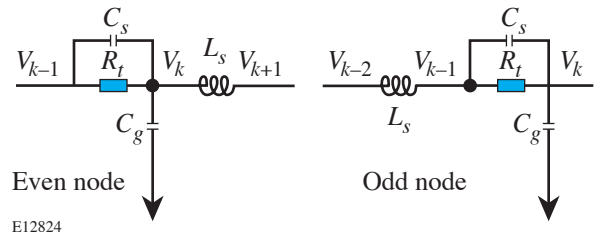


Figure 99.81 “Even” node and “odd” node of the lumped-element circuit. Here,  $R_t$  is the resistance of the small cell,  $C_s$  is the capacitance across the resistance,  $C_g$  is the capacitance between the cell and the ground,  $L_s$  is the inductance of the cell, and  $V_k$  is the potential at each node.

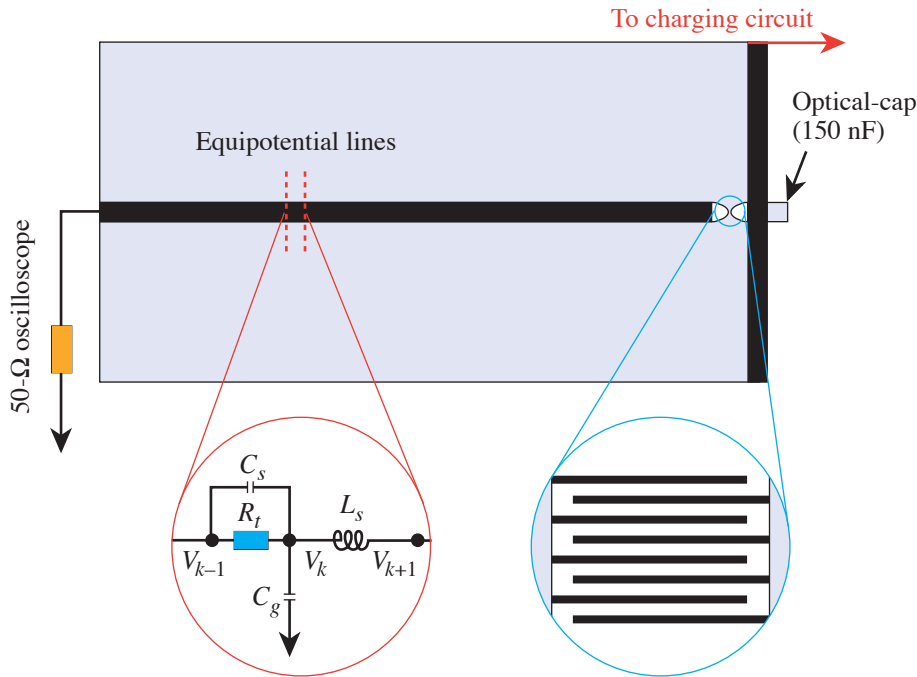


Figure 99.80 Top view of the broadband circuit designed for the MSM photodetectors. The one-dimensional transmission line was sliced into 1024 small cells along the equipotential lines and modeled as a lumped-element circuit as shown in the figure. To avoid an abrupt width change, a pad with a calculated curve tapers the transmission line down to the active area.

E12823

the 2-D structure can be degraded to a 1-D model. In the active region of the MSM photodiode, the gap between the finger electrodes was sliced into ten cells along the equipotential lines that follow the meandering shape of the fingers. When free carriers are generated optically in the gap, the carriers will move from one cell to the adjacent one under the external electric field. Transport perpendicular to the gap is ignored. Hence the time-dependent conductivity is 1-D between the finger electrodes. One concern about the 1-D model is that the electromagnetic waves may propagate along the fingers in real devices; however, the calculations show that the longest time for the electromagnetic wave to travel through the entire meander is less than 14 ps. This is small compared with the 40-ps rise time as shown below in the simulation results. Therefore, it is reasonable to ignore this propagation along the fingers and assume that the signal will travel from one finger electrode to the other finger electrode only so that the 1-D model is justified. The approach has an important advantage in that it allows the packaging circuit to be included in computing the response of the entire device assembly. A direct comparison with experimental results can then be made.

With the above assumptions, we can linearize the expressions for the currents and voltages in each cell. While the resistance in the metal transmission line is constant, the resistance in the semiconductor, which is a product of resistivity and length of the cell divided by the cross section of the cell, varies dynamically. The resistivity is calculated from the field-dependent expression

$$\rho(x,t) = \frac{1}{e[n(x,t)\mu_e(E) + p(x,t)\mu_h(E)]} (\Omega\text{cm}), \quad (1)$$

where the carrier densities  $n$  and  $p$  are calculated from the local optical intensity, absorption rate, and transport. The electron mobility  $\mu_e$ , a function of electric field, is given by Ref. 1, while the hole mobility  $\mu_h$  is fixed at 30 cm<sup>2</sup>/Vs. After optical illumination, the electrons and holes separate under the influence of the applied electric field and are collected by electrodes. The changing electric field and carrier densities cause the resistance of the cell to evolve in time. This change of the resistance is coupled out to other cells by changing the values of the voltage and current in each node. The transient response of the detector is then computed according to the distributed-circuit model.<sup>14</sup>

With  $V(t)$  as the voltage across the inductor at time  $t$  and  $V(t')$  as the voltage at the previous time  $t'$ , the currents at time  $t$  and  $t'$  in the inductor can be obtained by integrating  $V(t)$  and  $V(t')$  with the first-order Simpson's rule

$$\frac{1}{2}[V(t) + V(t')] = L_s \frac{dI}{dt} \approx \frac{L_s [I(t) - I(t')]}{\Delta t}, \quad (2)$$

where  $L_s$  is the inductance and  $\Delta t = t - t'$ . Similarly, the current at time  $t$  in the capacitor can be written as

$$I(t) = C \frac{V(t) - V(t')}{\Delta t}, \quad (3)$$

where  $C$  is the capacitance of a section of line of length  $\Delta x$ . In the simulation, the even nodes and odd nodes each generate a different set of equations. By applying Kirchhoff's law of current continuity, the circuit equation for the even nodes is

$$\begin{aligned} & V_k \left( \frac{C_g}{\Delta t} + \frac{\Delta t}{2L_s} + \frac{C_s}{\Delta t} + \frac{1}{R_t} \right) + V_{k+1} \left( -\frac{\Delta t}{2L_s} \right) \\ & + V_{k-1} \left( -\frac{C_s}{\Delta t} - \frac{1}{R_t} \right) \\ & = I'_k + V'_k \left( \frac{C_g}{\Delta t} - \frac{\Delta t}{2L_s} + \frac{C_s}{\Delta t} \right) + V'_{k+1} \left( \frac{\Delta t}{2L_s} \right) \\ & + V'_{k-1} \left( -\frac{C_s}{\Delta t} \right), \end{aligned} \quad (4)$$

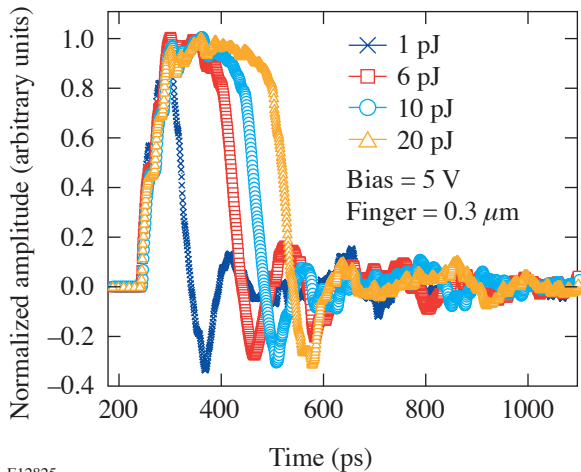
where  $k = 2n$  ( $n$  changes from 1 to 1024), symbols with prime mean the variables at previous  $t'$ , and symbols without prime mean the variables at present time  $t$ . Similarly, for the odd nodes we have



The initial values of current and voltage were determined from the dc-biased dark condition. These initial values were placed in matrix Eq. (6). The new values of voltage can then be solved. With the help of Eq. (2), the new values of current can be solved as well. Therefore, by iteration, the time response of the circuit can be numerically computed.

## Results and Discussion

In simulations, the model parameters were chosen to match the actual MSM-PD's previously tested.<sup>5</sup> The active area was  $50 \times 50 \mu\text{m}^2$ , and the finger width and spacing were both  $0.3 \mu\text{m}$ . For calculating the illumination on the detectors, we selected a Gaussian pulse with a full width at half maximum (FWHM) of 500 fs at a wavelength of 270 nm. Different illumination conditions with optical energies ranging from 0.01 pJ to 1 nJ were simulated. The results for optical pulse energies of 1, 6, 10, and 20 pJ are plotted in Fig. 99.82 with normalized amplitude. When the illumination level was lower than 1 pJ, the electric impulses delivered to the  $50\text{-}\Omega$  load had similar pulse shapes. The rising edge was dispersed by the transmission line and was typically 40 ps, which is longer than the optical pulse. The oscillations after the main peak were caused by the impedance discontinuities in the package. The shortest pulse width was 48 ps, which is a little shorter than our measured result of 60 ps for the same device as reported in Ref. 5. We attribute this discrepancy between simulation and measurement to parasitic effects not included in the



E12825

Figure 99.82

Simulated time responses of the detectors with different optical pulse energies of 1 pJ ( $\times$ ), 6 pJ (square), 10 pJ (circle), and 20 pJ (triangle) under 5-V bias. The amplitudes of the signal have been normalized to the peak values.

simulation, such as the connector discontinuities and the fact that in a microstrip transmission the field is not truly transverse electromagnetic.

The most-distinguishing feature of the results is that the pulse width broadens markedly as the optical pulse energy increases. This trend is the same as observed in experiments.<sup>5</sup> This increase in pulse duration can be attributed to the screening of the dark electric field between the finger electrodes by the space-charge field induced by the separation of the photogenerated electrons and holes. Qualitatively, at high excitation intensity, carrier densities of both electrons and holes increase to the point when the normally depleted region of the detector now has a substantial conductivity that temporarily decreases the electric field. As a result, the carriers are now swept out at a lower speed, hence the slower detector response. This effect is essentially the same as was found in GaAs photodetectors reported in Refs. 12 and 13.

## Comparison with Experiments

The pulse broadening, under high-level illumination, was observed in both experiments<sup>5</sup> and simulations. In this section the pulse width's dependence on the total optical energy will be compared for the two cases. In our simulations, the external quantum efficiency was assumed to be 100%; that is, each photon generates a free electron and hole pair. To compare the simulated and experimental results at the same illumination level, it is necessary to modify the optical pulse energy in experiments according to the measured external quantum efficiency, defined as the ratio of the number of the electron-hole pairs and the incident photons. The number of electrons generated by the optical pulse was obtained by integrating the photoelectric current; the number of photons in each optical pulse was determined by dividing the measured average laser power by the repetition rate (82 MHz for a Ti:sapphire laser) and the energy of each photon. In the case of the highest input of 391 pJ,  $\eta_{\text{ex}}$  was determined to be 1.77%. This factor was used to scale the experimental data. In Fig. 99.83, the simulated and measured FWHM's after the scaling are plotted together. With a single scaling factor, the experimental and simulated results are in close agreement.

Analysis of the data shows that the pulse width remains approximately constant until the optical energy exceeds a certain level (around 0.4 pJ) for both simulated results and scaled-experiment results. We can compute the photogenerated charge and compare its value to the stored charge in the device as follows: the capacitance of the MSM structure calculated to be  $0.182 \text{ pF}$ ,<sup>19</sup> corresponding to a stored charge

of  $9.1 \times 10^{-13}$  C (or, about  $5.7 \times 10^6$  electrons) given 5-V bias. At an optical energy of 0.4 pJ, the depletion region would have a total carrier density equal to about 10% of the stored charge. This amount appears to be the threshold of the onset of the space-charge effect.

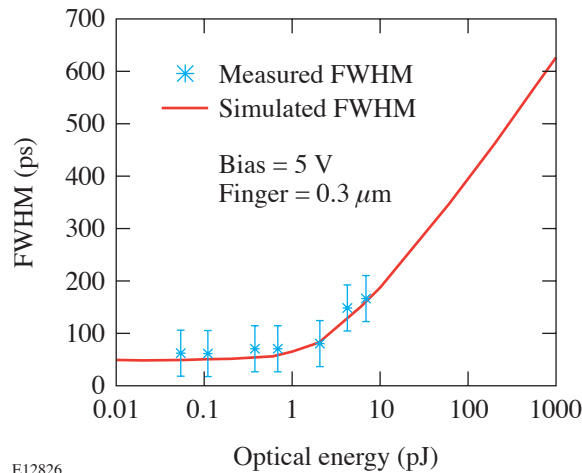


Figure 99.83  
Comparison of FWHM's from stimulation and experiment. To compare them in the same illumination level, a single factor was used to scale down the optical energy in experiment.

### Summary

In summary, a GaN interdigitized-finger MSMPD with 0.3- $\mu\text{m}$  finger width and spacing was packaged with a specially designed fast circuit. The entire assembly was simulated by a simplified, distributed-circuit approach so that the circuit effect can be conveniently monitored. The space-charge screening effect causing the broadening of the impulse response was discussed and compared with experimental results. After a single scaling factor of external quantum efficiency, theory and experiment were brought to a close agreement.

### ACKNOWLEDGMENT

This work was supported by the U.S. Department of Energy Office of Inertial Confinement Fusion under Cooperative Agreement No. DE-FC52-92SF19460, the University of Rochester, and the New York State Energy Research and Development Authority. The support of DOE does not constitute an endorsement by DOE of the views expressed in this article.

### REFERENCES

1. U. V. Bhapkar and M. S. Shur, *J. Appl. Phys.* **82**, 1649 (1997).
2. J. D. Albrecht *et al.*, *J. Appl. Phys.* **83**, 4777 (1998).
3. J. Kolnik *et al.*, *J. Appl. Phys.* **78**, 1033 (1995).
4. B. Gelmont, K. H. Kim, and M. Shur, *J. Appl. Phys.* **74**, 1818 (1993).
5. J. Li, W. R. Donaldson, and T. Y. Hsiang, *IEEE Photonics Technol. Lett.* **15**, 1141 (2003).
6. J. C. Carrano *et al.*, *J. Electron. Mater.* **28**, 325 (1999).
7. J. C. Carrano *et al.*, *Appl. Phys. Lett.* **73**, 2405 (1998).
8. D. Walker *et al.*, *Appl. Phys. Lett.* **74**, 762 (1999).
9. R. P. Joshi, A. N. Dharamsi, and J. McAdoo, *Appl. Phys. Lett.* **64**, 3611 (1994).
10. J. Li *et al.*, *Appl. Phys. Lett.* **84**, 2091 (2004).
11. K. Aliberti *et al.*, *Appl. Phys. Lett.* **80**, 2848 (2002).
12. S. V. Averine and R. Sachot, *IEE Proc., Optoelectron.* **147**, 145 (2000).
13. S. V. Averine and R. Sachot, *Solid-State Electron.* **44**, 1627 (2000).
14. L. Mu and W. R. Donaldson, in *Proceedings of the Ninth IEEE International Pulsed Power Conference*, edited by K. Prestwich and W. Baker (IEEE, New York, 1993), pp. 629–632.
15. L. E. Kingsley and W. R. Donaldson, *IEEE Trans. Electron Devices* **40**, 2344 (1993).
16. W. R. Donaldson and L. Mu, *IEEE J. Quantum Electron.* **30**, 2866 (1994).
17. B. C. Wadell, *Transmission Line Design Handbook* (Artech House, Boston, 1991).
18. S. M. Sze, D. J. Coleman, Jr., and A. Loya, *Solid-State Electron.* **14**, 1209 (1971).
19. Y. C. Lim and R. A. Moore, *IEEE Trans. Electron Devices* **ED-15**, 173 (1968).

